

Space Weather

RESEARCH ARTICLE

10.1029/2017SW001705

Key Points:

- Uncertainties in the atmospheric density result in uncertainties in the probability of collision
- Probability distribution functions of the probability of collision resulting from uncertainties in the atmospheric density are derived
- Monte Carlo procedures are used to compute the probability of collision

Correspondence to:

C. D. Bussy-Virat,
cbv@umich.edu

Citation:

Bussy-Virat, C. D., Ridley, A. J., & Getchius, J. W. (2018). Effects of uncertainties in the atmospheric density on the probability of collision between space objects. *Space Weather*, 16, 519–537. <https://doi.org/10.1029/2017SW001705>

Received 9 AUG 2017

Accepted 10 APR 2018

Accepted article online 27 APR 2018

Published online 18 MAY 2018

Effects of Uncertainties in the Atmospheric Density on the Probability of Collision Between Space Objects

Charles D. Bussy-Virat¹ , Aaron J. Ridley¹ , and Joel W. Getchius²

¹Department of Climate and Space Sciences and Engineering, University of Michigan, Ann Arbor, MI, USA, ²Omitron Inc., Beltsville, MD, USA

Abstract The rapid increase of the number of objects in orbit around the Earth poses a serious threat to operational spacecraft and astronauts. In order to effectively avoid collisions, mission operators need to assess the risk of collision between the satellite and any other object whose orbit is likely to approach its trajectory. Several algorithms predict the probability of collision but have limitations that impair the accuracy of the prediction. An important limitation is that uncertainties in the atmospheric density are usually not taken into account in the propagation of the covariance matrix from current epoch to closest approach time. The atmosphere between 100 km and 700 km is strongly driven by solar and magnetospheric activity. Therefore, uncertainties in the drivers directly relate to uncertainties in the neutral density, hence in the drag acceleration. This results in important considerations for the prediction of Low Earth Orbits, especially for the determination of the probability of collision. This study shows how uncertainties in the atmospheric density can cause significant differences in the probability of collision and presents an algorithm that takes these uncertainties into account to more accurately assess the risk of collision. As an example, the effects of a geomagnetic storm on the probability of collision are illustrated.

Plain Language Summary Spacecraft collision avoidance is particularly challenging at low altitudes (below 700 km). One of the main reasons is that, at these altitudes, satellite trajectories are strongly perturbed by atmospheric drag, a force particularly hard to model. The sources of errors mostly come from the complex coupling between the Sun and the Earth's environment. This system drives the density of the Earth's atmosphere on which the atmospheric drag directly depends. In other words, uncertainties in the atmospheric density result in large uncertainties in the satellite trajectories. The probability of collision, which is computed from the prediction of the satellite trajectories, thus cannot be predicted perfectly accurately. However, mission operators decide whether or not a collision avoidance maneuver has to be carried out based on the value of the probability of collision. Therefore, it is essential to characterize the level of uncertainty associated with the prediction of the probability of collision. The research presented here offers an approach to determine the uncertainty on the prediction of the probability of collision as a result of uncertainties in the atmospheric density. The ultimate goal is to assist mission operators in making the correct decision with regard to potential collision avoidance maneuvers.

1. Introduction

The population of objects in orbit around the Earth has dramatically increased in the past decade. In April 2005, National Aeronautics and Space Administration (NASA) performed its first collision avoidance maneuver on a robotic spacecraft (Terra satellite). Two years later, the Chinese satellite Fengyun-1C was destroyed, causing the largest increase in debris in space history (about 3,000 objects larger than 10 cm). On 10 February 2009, the collision between the operational communication satellite Iridium 33 and the retired Russian communication satellite Cosmos 2251 generated 2,000 debris larger than 10 cm, with many thousands of smaller pieces at an altitude of 800 km. In 2015, four collision avoidance maneuvers and one “shelter-in-Soyuz” procedure were performed by the International Space Station (Liou, 2016; Newman, 2016).

Collision avoidance requires the knowledge of the position and velocity of all objects in orbit. Some satellite mission operators can keep track of their satellites quite accurately using Global Positioning System data, but the trajectories of other orbiting objects are harder to accurately specify. Space Situational Awareness

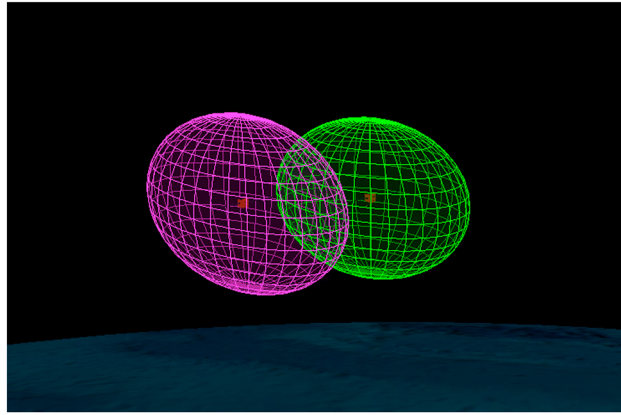


Figure 1. Ellipsoids surrounding the primary and secondary spacecraft to represent the uncertainties in the positions of each object (Satellite Tool Kit - Analytical Graphics, Inc.).

refers to the effort of gathering and updating the trajectories of natural and man-made orbiting objects (Stoll et al., 2013). Two of the organizations that support the Space Situational Awareness process are the Joint Space Operations Center (JSpOC), part of the eighteenth Space Control Squadron, and the Space Data Association. The Space Data Association was established for satellite operators to share the most up-to-date satellite data (Stoll et al., 2013). JSpOC is currently the single full-time global provider of object positions used in collision avoidance due to the accuracy and timeliness of the available information (Aida et al., 2015). It tracks more than 23,000 objects to evaluate the risk of collision with operating satellites by looking for any close approach with cataloged objects. If a potential conjunction is predicted by JSpOC, a Conjunction Data Message (CDM) is generated, which includes information about the close approach to alert the mission operator of a possible encounter. To evaluate the risk of collision, the probability of collision P_c is calculated based on the covariance matrices and the states of both objects at the Time of Close Approach (TCA). This step is part of the Conjunction Assessment Risk Analysis (CARA).

In order to perform CARA, the probability of collision must be accurately determined. This is done by comparing the covariance matrices of the two objects at the time of closest approach. A covariance matrix represents the uncertainties in the state of the object. The i th diagonal element corresponds to the variance of the i th parameter (square of the standard deviation). The off-diagonal element i, j is proportional to the correlation coefficient between the i th and the j th elements. The position portion of the covariance matrices of each of the two objects can be represented by an ellipsoid, with an orientation given by the principal axes of the covariance matrix. Two such ellipsoids are illustrated in Figure 1.

The volume of intersection of the two ellipsoids is a representation of the probability of collision of the two objects. Computing this intersection volume implies calculating a three-dimensional integral, which can be computationally intense and complex. Therefore, the relative motion is assumed to be rectilinear, and the derivation can be reduced to a two-dimensional integral in the plane normal to the relative velocity vector, called the conjunction plane (Hejduk & Frigm, 2015; Sanchez-Ortiz et al., 2015). Moreover, the orbit uncertainties of the primary object are assumed to be uncorrelated with the orbit uncertainties of the secondary object, so the two covariance matrices can be combined in a single covariance matrix (Chan, 2008). Finally, the position uncertainties of the two objects are assumed constant during the encounter, so the combined covariance matrix is constant during the close approach. These assumptions are valid if the duration of the encounter is short enough (< 500 s) or equivalently if the relative velocity between the primary and secondary objects is high enough (> 10 km/s) (Hejduk & Frigm, 2015). The probability of collision, P_c , is then expressed as (Akella & Alfried, 2000; Alfried et al., 1999; Foster, 2001; Sanchez-Ortiz et al., 2015)

$$P_c = \frac{1}{2\pi\sqrt{\det(C)}} \int_{-R}^R \int_{-\sqrt{R^2-x^2}}^{\sqrt{R^2-x^2}} e^{-\frac{1}{2}\vec{r}^T C^{-1} \vec{r}} dz dx \quad (1)$$

where R is the sum of the two object radii, \vec{r} the vector between the point of interest in the conjunction plane, and each point (x, z) is in the circle of radius R (integration area). Most of the satellites do not have a spherical shape, in which case their radius can be defined as their largest dimension.

Others have modified this technique. Patera (2001) used the symmetric form of the probability density to reduce the 2-D integral to a 1-D contour integral. The contour corresponds to the perimeter of the 2-D integration area. This method provides an easier numerical implementation and is computationally faster. Patera (2005) used numerical quadrature techniques to transform the contour integral to a 1-D angular integral by shifting the origin of the coordinate system. Alfano (2005a) reduced the 2-D integral into a 1-D integral using the error function and analyzed it applying the Simpson's one-third rule. Chan (2008) introduced the Rician function to approximate the 2-D integral as a 1-D integral over a circle with an area equivalent to the elliptical cross-section area.

Although these methods are numerically easy to implement and computationally efficient, they rely on multiple assumptions that do not necessarily hold in every conjunction case. Alfano (2009) assessed Patera's and Alfano's methods for linear relative motion and showed important differences with the baseline Monte Carlo method, particularly when the relative motion assumption does not hold, where errors up to 60% were found. Other methods, which do not assume linear relative motion (adjoining cylinders's method, Alfano, 2005b; bundled parallelepipeds's method, Alfano, 2005b; and method of voxels, Alfano, 2006) also resulted in large errors because of limiting assumptions. Monte Carlo procedures do not require the relative motion to be linear or the covariance matrices to be constant during the encounter. Therefore, the collision risk assessment can be more accurate in theory. The main drawback of the Monte Carlo approach is that it is computationally intensive. This method is presented in detail in section 2.

Alfriend et al. (1999) investigated the sensitivity of the probability of collision to errors in the covariance matrix and to the encounter geometry. The study underlined the fact that although the position covariance at epoch is accurate, the velocity covariance is too optimistic because it assumes the dynamic model is perfect. Specifically, the uncertainties in the atmospheric density are usually not taken into account. As a result, when such uncertainties are not considered, the position uncertainties at the time of close approach are too optimistic by about an order of magnitude. Alfriend et al. (1999) showed that small errors in the covariance matrix can cause important changes in P_c .

At low Earth orbit (LEO) altitudes, one of the main forces acting on spacecraft and debris is atmospheric drag and is a perturbing force particularly hard to model and predict. The drag acceleration \mathbf{a}_{drag} of a simple surface is represented by (Vallado & McClain, 2007)

$$\mathbf{a}_{\text{drag}} = -\frac{1}{2} \frac{C_D A}{m} \rho v_{\text{rel}}^2 \frac{\mathbf{v}_{\text{rel}}}{v_{\text{rel}}} \quad (2)$$

where C_D , A , and m are the drag coefficient, area projected toward the velocity vector, and mass of the surface, respectively, and \mathbf{v}_{rel} is the satellite velocity with respect to the moving atmosphere of density ρ . The thermosphere is too dense to be neglected in accurate orbit calculations, particularly below ~ 500 km. The atmosphere above about 100 km is strongly coupled to the space environment. This system is very complex and the response of the density to driving from the ionosphere, magnetosphere, and Sun is very challenging to estimate. Moreover, the drivers of entire near-Earth space environment, mainly linked to solar activity, are themselves difficult to predict. Proxies are used to model these drivers, such as F10.7. This is the solar radio flux at a wavelength of 10.7 cm, and it is commonly used to model extreme ultraviolet (EUV) irradiance (Emmert, 2015). The perturbations of the Earth's magnetic field resulting from its interaction with the interplanetary magnetic field (IMF) and the solar wind particles are described by magnetic activity indices such as Kp, Ap, disturbance storm time (Dst), and auroral electrojet (AE). These indices can be derived from magnetic perturbations directly measured from stations on Earth.

Very few studies have analyzed the impact of uncertainties in the atmospheric drag, despite the fact that it is the largest source of errors for LEO orbits (Emmert et al., 2016; Storz et al., 2005). By modeling the errors in EUV 10-day forecasts with a Brownian motion process, Emmert et al. (2014, 2016) derived an analytical equation that relates the uncertainties in F10.7 to uncertainties in the in-track position and found that the in-track position errors grow with time as $\sim t^5$. Although an analytical equation saves a lot of computational time, it does not provide a solution accurate enough for collision risk assessment. In particular, the solution assumes that the only perturbing force is atmospheric drag. However, neglecting the other perturbations can lead to important errors, in particular, if neglecting the asphericity of the Earth. In addition, the effects of errors in the prediction of the solar proxies increase dramatically in the presence of a solar storm.

Pachura and Hejduk (2016) showed that a miss prediction of a geomagnetic event leads to important changes in the probability of collision, up to a few orders of magnitude.

This study first presents an improvement of the Spacecraft Orbital Characterization Kit (SpOCK) to accurately predict the probability of collision between two space objects using Monte Carlo procedures. The algorithm models all perturbing forces and takes into account uncertainties in both F10.7 and A_p . The goal is to show how uncertainties in solar driver predictions result in important errors in the probability of collision. Additionally, the effects of a miss prediction of a geomagnetic storm on the probability of collision are demonstrated in an example. The algorithm developed can be used in real time and can provide mission operators with a better estimation of the risk of collision.

2. Methodology

The central capability of SpOCK is a high-accuracy numerical propagator of spacecraft orbits using a comprehensive model of the dynamics of spacecraft in orbit, including the asphericity of the Earth, atmospheric drag acceleration, solar radiation pressure, and gravitational perturbations from the Moon and the Sun. Specifically, the nonspherical portion of the mass distribution of the Earth is modeled with a decomposition in spherical harmonics of the gravitational potential. Thermospheric models (Naval Research Laboratory Mass Spectrometer Incoherent Scatter Radar Extended [NRLMSISE], Picone et al., 2002, and the Global Ionosphere Thermosphere Model, Ridley et al., 2006) are implemented in SpOCK to derive the atmospheric density at the position of the spacecraft and the time of interest, allowing for an accurate representation of the atmospheric drag. In addition to modeling the motion of satellites, SpOCK includes several functionalities, such as the coverage of ground stations, the computation of solar power, and the storm intersection forecast tool developed for the Cyclone Global Navigation Satellite System mission. Developed in C, SpOCK supports parallelism and is therefore well suited for ensemble, Monte Carlo, or satellite constellation analysis. The algorithm and its different functionalities are presented in Bussy-Virat et al. (2018).

2.1. CARA Algorithm

SpOCK can assess the risk of collision with other space objects in orbit (operational satellites or debris). Monte Carlo procedures are used to perturb the initial epoch state (position and velocity) of the primary and secondary spacecraft from the covariance matrices. The algorithm does not have to make any assumptions about the relative motion, the uncertainties in motion, or the covariances during the time span.

SpOCK is initialized with the state (position and velocity) and the covariance matrices of both space objects (noted \bar{O}_1 and \bar{O}_2) in the Earth Centered Inertial (ECI) J2000 coordinate system (6×6 matrices). The sum of the two object radii, $D_{\text{collision}}$, and the threshold distance under which a close approach is flagged, D_{CA} , as well as the number of ensembles used in the Monte Carlo procedures, noted N_e , are also input.

The flow diagram in Figure 2 illustrates the process to evaluate the risk of collision that leads to the determination of the probability of collision between the two space objects.

2.1.1. Close Approach Between the Unperturbed Orbits

The first step in determining the probability of collision between two objects is to explore whether the orbits overlap. A first filter rules out the possibility of an encounter if the perigee of the higher object's orbit is greater than the apogee of the lower object's orbit. If this is not the case, the altitudes cross at some point, and the secondary object could present a potential threat. In that case, the two orbits are propagated to explore potential close approaches. The propagator uses a Fourth Order Runge-Kutta (RK4) method with a fixed time step dt to integrate the acceleration and velocity at each time step t_i of the simulation. A close approach is defined as any minimum in the distance between the two objects smaller than a specified distance, D_{CA} . To determine if a minimum occurs in each interval $[t_i, t_{i+1}]$, SpOCK uses a similar algorithm as Alfano-Negron Close Approach Software (Alfano, 1994). The flow diagram for this algorithm is presented in a separated block from the rest of the flow diagram in Figure 2 (black block at the bottom of the figure). First, it looks for the existence of a minimum in the distance between the objects by modeling the time derivative of the distance between the two objects by a third-order polynomial, P_d , and assessing if any real root t_{root} exists in the interval $[t_i, t_{i+1}]$. The additional condition $\frac{dP_d(t_{\text{root}})}{dt} > 0$ ensures that the root corresponds to a minimum and not a maximum (not represented in Figure 2). If a root is found in the interval $[t_i, t_{i+1}]$, the algorithm then determines the Distance of Close Approach (DCA) at t_{root} (now noted as TCA). The relative vector between the secondary and the primary objects is noted $\mathbf{r}_d = \mathbf{r}_2 - \mathbf{r}_1$. SpOCK models the components $r_{d,x}$, $r_{d,y}$, and $r_{d,z}$ by fifth-order polynomials

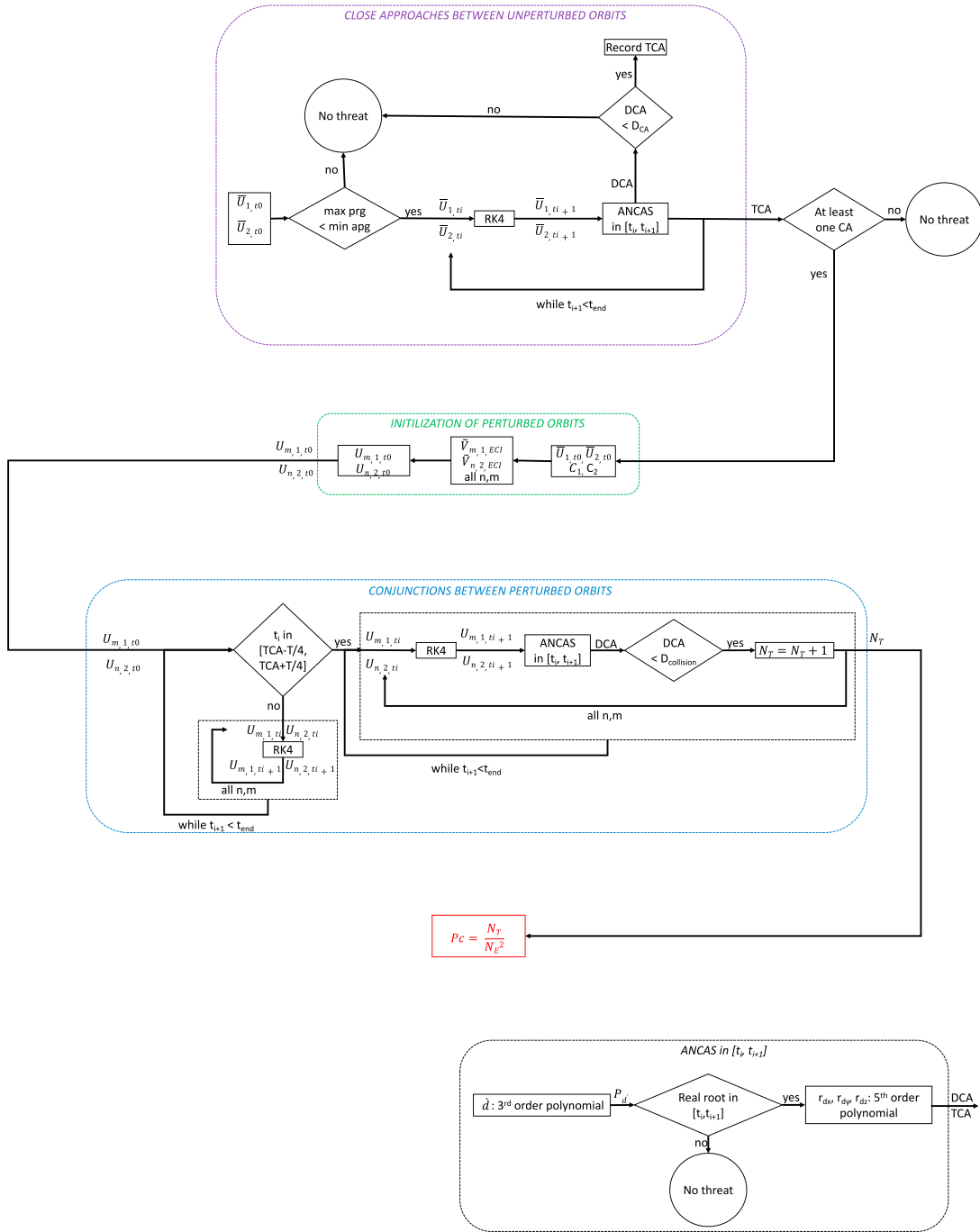


Figure 2. Flow diagram of SpOCK's Conjunction Assessment Risk Analysis algorithm. DCA = Distance of Close Approach; ECI = Earth Centered Inertial; TCA = Time of Close Approach; ANCAS = Alfano-Negron Close Approach Software.

$P_{r_{dx}}, P_{r_{dy}}$, and $P_{r_{dz}}$. The distance at close approach is then expressed as

$$DCA = \sqrt{P_{r_{dx}}^2 + P_{r_{dy}}^2 + P_{r_{dz}}^2} \quad (3)$$

If $DCA < D_{CA}$, then the situation is recorded as a close approach.

This operation is repeated for each interval $[t_i, t_{i+1}]$ of the propagation.

2.1.2. Initialization of Perturbed Orbits

If a close approach between the two unperturbed orbits is found, there is a potential risk for a collision. In that case, the Monte Carlo process is initialized at t_0 (green diagram second to top of Figure 2). The initialization consists in perturbing the ECI states of the primary and secondary objects (\bar{U}_{1,t_0} and \bar{U}_{2,t_0}). First, the covariance matrices (noted C_1 for the primary object and C_2 for the secondary object) are diagonalized and the two sets of six eigenvalues derived. For each set of eigenvalue, N_e random vectors (6×1 for the position and the velocity) are generated following a normal distribution centered around 0 with a standard deviation equal to the square root of the eigenvalue of the covariance matrix:

$$\tilde{V}_{m,j} = \begin{pmatrix} \text{randn}(0, \sqrt{\lambda_{1,j}}) \\ \text{randn}(0, \sqrt{\lambda_{2,j}}) \\ \text{randn}(0, \sqrt{\lambda_{3,j}}) \\ \text{randn}(0, \sqrt{\lambda_{4,j}}) \\ \text{randn}(0, \sqrt{\lambda_{5,j}}) \\ \text{randn}(0, \sqrt{\lambda_{6,j}}) \end{pmatrix}$$

where $\tilde{V}_{m,j}$ represents the m th random vector ($m = 1, \dots, N_e$) associated with the primary ($j = 1$) or secondary ($j = 2$) object, and $\lambda_{i,j}$ the i th eigenvalue ($i = 1, \dots, 6$) of the covariance matrix C_j .

Each vector $\tilde{V}_{m,j}$ is then converted back to the ECI coordinate system ($\tilde{V}_{m,j,\text{ECI}}$) with the rotation matrix used for the diagonalization of the covariance matrix.

Finally, each perturbation $\tilde{V}_{m,j,\text{ECI}}$ is added to the unperturbed ECI state to generate N_e perturbed states $U_{m,1}$ and $U_{n,2}$:

$$U_{m,1,t_0} = \bar{U}_{1,t_0} + \tilde{V}_{m,1,\text{ECI}} \quad (4)$$

$$U_{n,2,t_0} = \bar{U}_{2,t_0} + \tilde{V}_{n,2,\text{ECI}} \quad (5)$$

Each ensemble member initialized as U_{m,j,t_0} is now noted $O_{m,j}$.

2.1.3. Conjunctions Between the Perturbed Orbits

Once the $2N_e$ perturbed orbits are initialized, SpOCK propagates them (blue block third to top in Figure 2). During the propagation, it screens for any conjunction between a perturbed ensemble member $O_{m,1}$ ($m = 1, \dots, N_e$) of the primary object and a perturbed ensemble member $O_{n,2}$ ($n = 1, \dots, N_e$) of the secondary object. The algorithm is the same as the one to find a close approach between the unperturbed orbits \bar{O}_1 and \bar{O}_2 . However, it now uses the sum of the two object radii $D_{\text{collision}}$ as the minimum distance under which a conjunction is recorded. Therefore, SpOCK first looks for the existence of a minimum distance in each interval $[t_i, t_{i+1}]$, in which case it then calculates the minimum distance as in equation (3). If this distance is smaller than $D_{\text{collision}}$, the situation is recorded as a collision. SpOCK repeats this operation for each combination in the set (m, n) resulting in N_e^2 comparisons. The total number of collisions found is noted N_T .

To be computationally efficient, conjunctions between each perturbed orbit $O_{m,1}$ and $O_{n,2}$ are not screened in every interval $[t_i, t_{i+1}]$ of the propagation but only in a time spanning the unperturbed close approach determined in the first step of CARA. This time span is equal to half an orbital period T to ensure that no collision is missed between the perturbed orbits. If several close approaches were found, then SpOCK applies this algorithm for each interval $[TCA - T/4, TCA + T/4]$.

2.1.4. Derivation of the Probability of Collision

Once the $2N_e$ orbits are propagated and screened for collisions, the probability of collision is calculated as the ratio between the total number of collisions N_T divided by the total number of possible scenarios N_e^2 (red block fourth to top in Figure 2):

$$P_c = \frac{N_T}{N_e^2} \quad (6)$$

This algorithm, presented in Alfano (2009), is commonly referred as the all-to-all strategy, as opposed to the one-to-one strategy that compares the position of each object $O_{m,1}$ to a single object $O_{n,2}$. It provides accurate

estimates of the probability of collision in a reasonable computational time, although an accurate value of the confidence interval should be computed using other methods, such as the one-to-one strategy (Schilling et al., 2016). If the one-to-one method was employed to compute the probability of collision though, it would involve the orbit propagation of more ensemble members, which would require a longer run time (or the use of more cores) and would make this solution not easily applicable for operations. Therefore, an empirical method for the determination of the confidence interval was used in this study to verify that the number of ensemble members considered was large enough to get an accurate estimation of P_c using the Monte Carlo approach. The 50,000 ensemble members for each object were considered, which corresponded to a total number of possible scenarios N_e^2 of 2.5 billions. To be computationally efficient, SpOCK runs the ensemble members in parallel, allowing the risk assessment of a 2-day scenario to be performed in an hour using 200 cores.

2.2. Modeling Uncertainties in F10.7 and Ap

The uncertainty in the thermospheric density modeling is generally of the order of 10–15% (Vallado & Finkleman, 2014). This is when considering a perfect knowledge of the inputs used in the thermosphere models, such as the solar flux F10.7, Ap, or Dst. However, predicting the solar drivers a few days ahead adds more uncertainties in the prediction of the thermospheric density. The large variability of the solar activity makes the task even harder. Geomagnetic activity driven by solar flares, coronal mass ejections, and corotating interaction regions (CIRs) causes the most important disturbances of the neutral density. For example, it was found that CIRs can cause density increases by 75% on average (Lei et al., 2011). A 30% to 60% increase at low latitude to midlatitude in the density response to EUV solar flux enhancement resulting from a solar flare was reported in Sutton et al. (2006) and Pawlowski and Ridley (2011). Bruinsma et al. (2006) and Sutton et al. (2005) studied the response to severe geomagnetic storms. Both noted a rapid response of the thermospheric density (approximately a few hours) at all latitudes with enhancements by more than 3 times the density. Bruinsma and Forbes (2007) reported up to 800% density enhancements at the equator during sudden increases in geomagnetic activity.

Despite these considerations, collision risk assessment is usually performed by neglecting the uncertainties in the atmospheric density, although it recently became a standard practice for the Department of Defense (DoD) to include atmospheric density errors in the covariance through the use of a consider parameter. At LEO altitudes, where atmospheric drag is the dominant perturbation, neglecting such uncertainties can result in important errors in the probability of collision.

SpOCK primarily uses the NRLMSISE density model to derive the density at the position of the spacecraft at each time step of the propagation. The solar inputs of NRLMSISE are the solar flux F10.7 and the geomagnetic index Ap. These are predicted in real time for the following 45 days at the Space Weather Prediction Center (SWPC) from the National Oceanic and Atmospheric Administration. To model uncertainties in the predictions of F10.7 and Ap, historical predictions (noted $P_{\text{predicted}}$, where P is F10.7 or Ap) over 2 years were compared to actual measurements (noted P_{measured}) as a function of prediction horizon. For each forecast time (1–3 days ahead), the difference between the predicted index and the measured value was computed ($P_{\text{predicted}} - P_{\text{measured}}$), from which distributions were derived. Figure 3 shows the probability distribution function (PDF) of the F10.7 prediction error (top left) and the Ap prediction error (bottom left) for a 2-day forecast horizon. For every prediction horizon, each distribution is segmented in seven bins from –15 to 15. For example, there is a 7% chance that the error on the prediction of F10.7 after 2 days is ~9 (red bin in top distribution) and there is a 35% chance that the prediction of Ap is correct (green bin in bottom distribution). Although the distributions vary with the prediction horizon, since the accuracy of the forecast degrades for longer prediction horizons, the PDFs are all centered around 0, indicating that the SWPC predictions were nonbiased.

SpOCK uses these PDFs to model the uncertainties in the predictions of F10.7 and Ap. Each graph on the right of Figure 3 shows an example of the seven different 3-day predictions of F10.7 (top) and Ap (bottom) on 26 November. A given prediction is derived as the sum of the value at the center of a bin in the PDF (reported in the legend) with the predicted value by SWPC. For instance, SWPC predicted F10.7 to be 83 and Ap to be 9 on 28 November. Therefore, the prediction of F10.7 corresponding to the red bin centered at 9 was 91. Similarly, the prediction of Ap corresponding to the light blue bin centered at –4 was 5. Applying this approach for each prediction horizon (1–3 days ahead), SpOCK generated a series of predictions for F10.7 and Ap.

The Pearson correlation and the Kendall's tau coefficients of the historical forecast errors on F10.7 and Ap were, respectively, 0.02 and 0.009, indicating that they were uncorrelated. Therefore, the F10.7 and Ap predic-

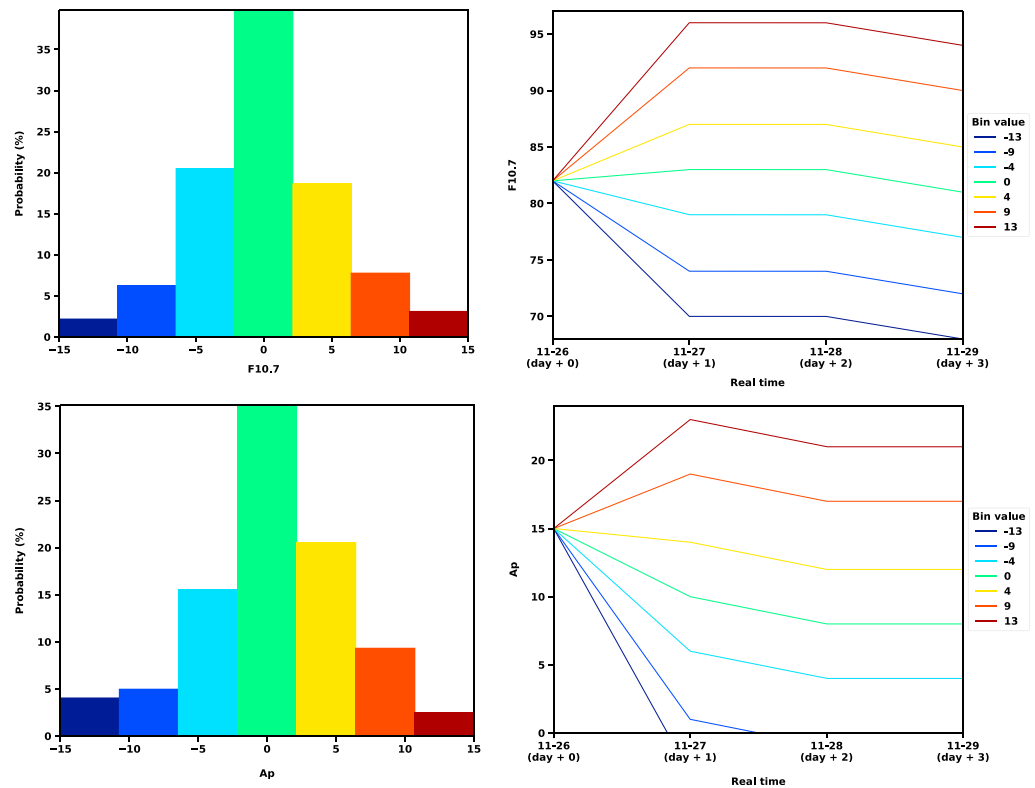


Figure 3. Probability distribution functions of the error in historical forecast of F10.7 (top left) and Ap (bottom left). Prediction of the solar flux F10.7 (top right) and geomagnetic index Ap (bottom right) as a function of forecast time derived from these PDFs and the prediction by SWPC.

tion errors were varied independently and input in NRLMSISE to model uncertainties in the prediction of the atmospheric density. Specifically, 7×7 different combinations from the PDFs of the F10.7 and Ap prediction errors resulted in 49 density scenarios. The density modeled with NRLMSISE from these different solar activity conditions at a theoretical satellite location (at 400 km) is shown in Figure 4.

SpOCK uses real-time predictions from SWPC and adds uncertainties to assess the risk of collision under different solar conditions. SpOCK propagates different ensembles, consisting of thousands of members, through different thermospheres. Each individual ensemble is propagated through NRLMSISE driven by the same

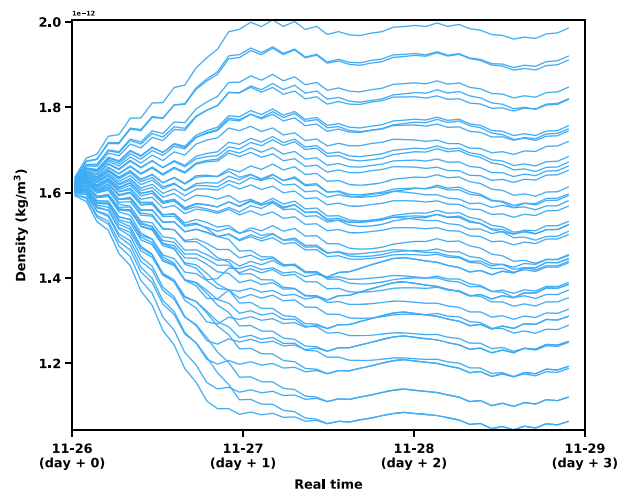


Figure 4. Atmospheric density at the position of the spacecraft as a function of forecast time modeled by NRLMSISE from the probability distribution functions of the errors in historical F10.7 and Ap forecast (shown in Figure 3).

drivers, so the members can be realistically compared to each other. Different ensembles represent different density drivers, such that the dependence of the probability of collision on the density drivers can be explored. These simulations are run in parallel, which enables a quick evaluation of the range of possible values of the predicted probability of collisions, instead of one unique value as it is currently done in a typical conjunction risk assessment analysis.

2.3. Modeling Other Uncertainties

When assessing the true risk of collision, all uncertainties must be taken into account. Uncertainties in the initial position and velocity are important because of the limited availability and accuracy of tracking the object. The thermospheric density is the main source of uncertainties in the propagation of the spacecraft but, as shown in equation (2), it is not the only parameter of the drag acceleration. Uncertainties in the drag coefficient and the cross-section area are also important. The drag coefficient and the cross-section area depend on the attitude of the satellite, so they are sometimes combined into one single parameter, such as the ballistic coefficient ($B_C = \frac{C_D A}{m}$). However, uncertainties in both parameters can be modeled separately in SpOCK. For most secondary objects with unknown drag coefficients and cross-section areas, the Monte Carlo procedures should include directly perturbing the ballistic coefficient from its variance estimated in the covariance matrix.

The coefficient of drag C_D represents the transfer in momentum between the molecules of the atmosphere and the surfaces of the satellite. It is a function of the satellite shape and attitude, of the atmospheric conditions (temperature and composition), and of the properties of the satellite surfaces. It usually decreases with the altitude (Horsley, 2012; Moe & Moe, 2005). In order to model uncertainties in the drag coefficient, SpOCK initializes the properties of each surface of the ensemble members with drag coefficients computed from the covariance matrix at the initial epoch.

Modeling the uncertainty in the attitude for a controlled satellite that has a known attitude control uncertainty consists in having ensemble members that drift with a random angular velocity from a nominal attitude for a given time before going back to the nominal attitude. This enables the simulation of the attitude determination and control system of satellites that randomly drift from a nominal controlled attitude. Additionally, objects that are uncontrolled can be simulated by setting nominal tumbling rates around the three axes, with uncertainties around those nominal rates also specified.

Although these different uncertainties need to be taken into account in a realistic collision risk assessment, this study focuses on exclusively modeling uncertainties in the initial positions and velocities, as well as in the thermospheric density.

3. Validation

To validate the conjunction assessment risk analysis algorithm in SpOCK, the cumulative probabilities of collision computed for three different cases were compared with results from Alfano, 2009. More specifically, two LEO configurations (Cases 6 and 7 in Alfano, 2009) and one GEO configuration (Case 1 in Alfano, 2009) were analyzed. The initial states and covariance matrices, included in Alfano (2009), were used to initialize CARA in SpOCK. Alfano (2009) used a similar CARA algorithm as SpOCK. In all three cases, the time of close approach is 2 days after the epoch. The dynamic model used a spherical Earth with no perturbations, since the goal of this study was to validate the algorithm for computation of the probability of collision, while SpOCK's propagator and its dynamic model were validated in a previous study (Bussy-Virat et al., 2018).

Figure 5 shows the cumulative distribution functions (CDFs) computed by SpOCK for Cases 1 (top), 6 (center), and 7 (bottom). Similar figures are available in Alfano (2009) but are not shown here because they correspond to probabilities determined with a different method than the Monte Carlo approach. Therefore, a direct comparison of the cumulative probability as a function of time is not possible. However, the trends of the figures in Alfano (2009) are very similar to the ones presented in Figure 5. Case 1 represent a nonlinear relative motion that causes the probability to increase again a few hours after the first close approach. Cases 6 and 7 correspond to a linear relative motion where the probability of collision starts growing a few minutes before the unperturbed close approach, with a faster increase for Case 6. The text in each plot summarizes the results for the cumulative probability of collision calculated by SpOCK and compared to the value in Alfano (2009).

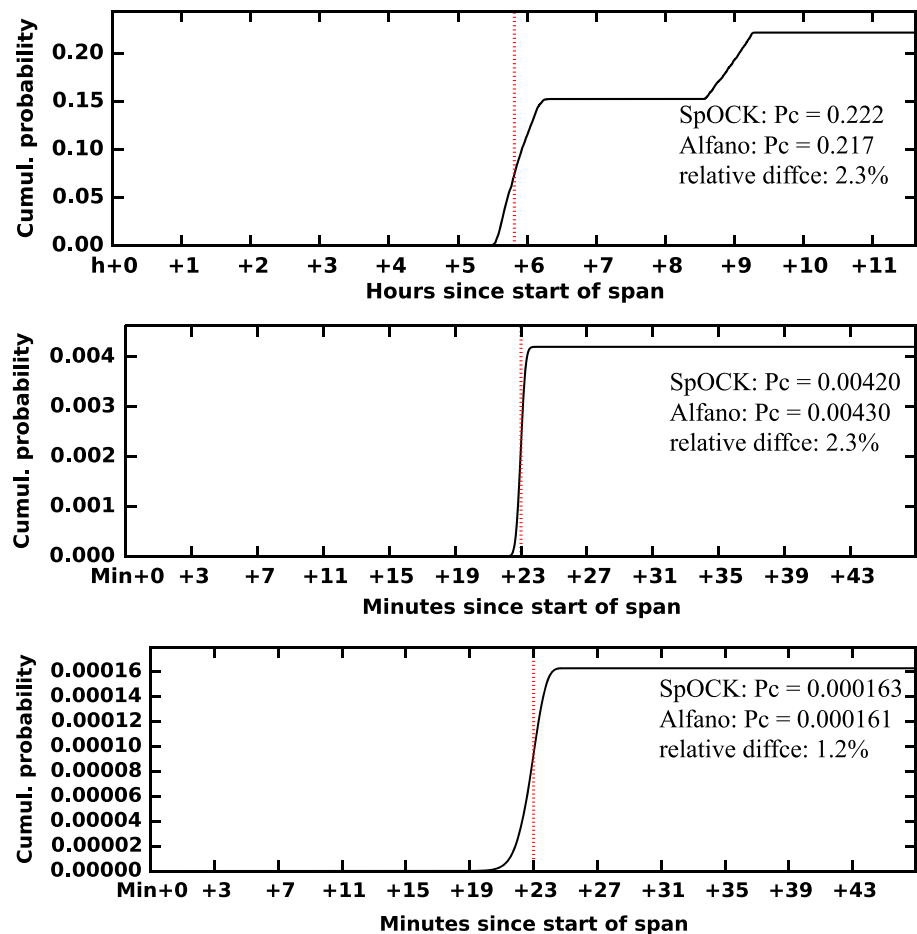


Figure 5. Cumulative probability of collision during the half orbit spanning the unperturbed close approach. The vertical red dashed line represents the time of close approach between the two unperturbed orbits. The initial states and covariance matrices are taken from Alfano (2009): top is Case 1, center is Case 6, and bottom is Case 7. SpOCK = Spacecraft Orbital Characterization Kit.

The relative difference is smaller than 3% for the three cases, proving that both algorithms are in good agreement. The small differences might be due to the fact that Alfano (2009) used an analytic equation to propagate the covariance matrices from current epoch to time of closest approach.

4. Results and Discussion

4.1. Effects of Atmospheric Drag on the Probability of Collision

To understand the effects of atmospheric drag on the probability of collision, a hypothetical collision between two satellites with slightly different velocities is considered. Both spacecraft start at their respective initial position, and Satellite 2 is assumed to have the higher speed of the two satellites. The distance between the initial positions and the conjunction point is, respectively, noted D1 and D2.

If the density of the atmosphere was actually higher than predicted, the increase in atmospheric drag would have more effect on Satellite 2 than on Satellite 1 because Satellite 2 is moving faster. In other words, the altitude of Satellite 2 would decrease faster than the altitude of Satellite 1, so the speed of Satellite 2 would increase more than the speed of Satellite 1. Therefore, Satellite 2 would reach the distance D2 before Satellite 1 reached the distance D1. Because of this differential change in speed, Satellite 2 would get to the conjunction point before Satellite 1, so the two satellites would potentially not collide anymore. Similarly, two spacecraft that were not predicted to collide could actually collide if the density was different from the prediction.

In the Monte Carlo method, a large number of such situations are considered. The total number of collisions in the Monte Carlo procedure therefore directly depends on the density of the atmosphere in which the

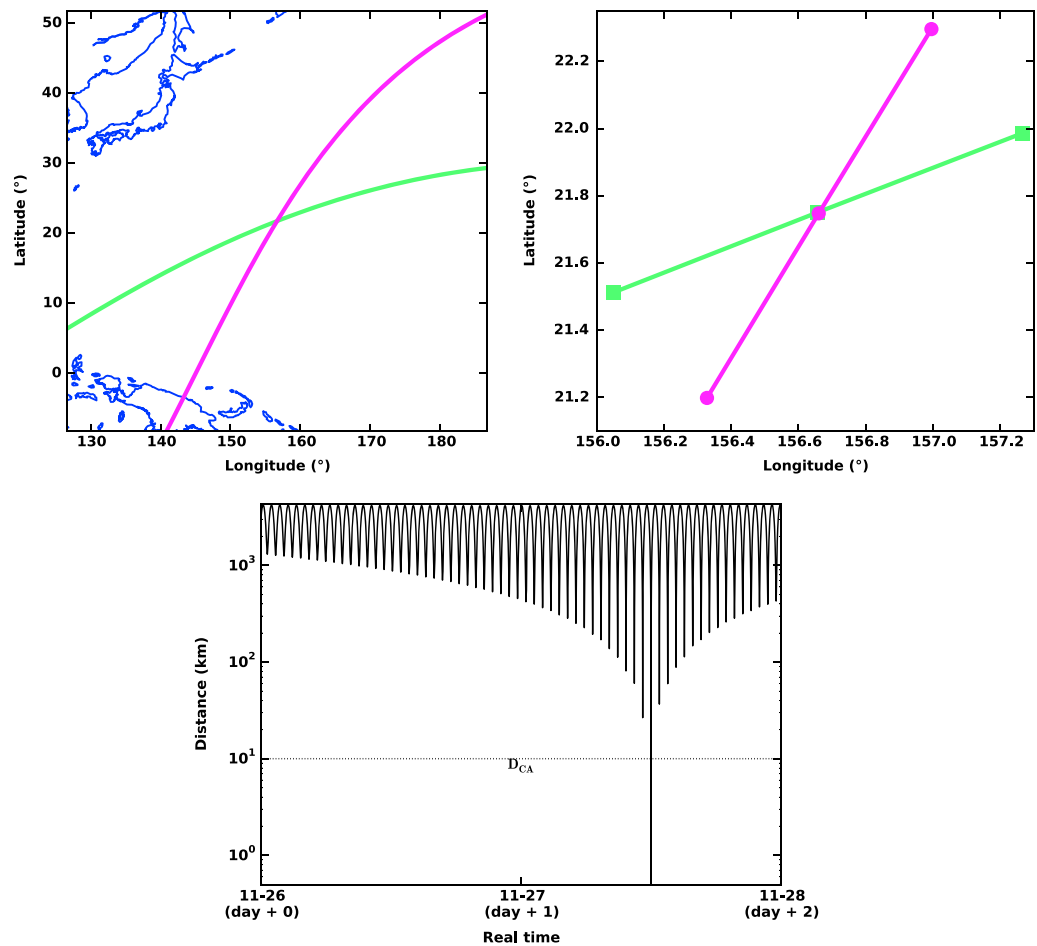


Figure 6. (top row) Two-dimensional visualization of the two orbits. Satellite 1 (green line) orbits at 400 km with a 30° inclination and a 0° RAAN. Satellite 2 (magenta line) orbits at 400 km with a 60° inclination and a 30° RAAN. The right figure is a zoom in over a $\sim 120 \text{ km} \times 120\text{-km}$ region. (bottom) Distance between the two unperturbed orbits over the first 2 days of the propagation. The close approach occurs on 27 November at 12 p.m. The threshold distance for close approaches, D_{CA} , is indicated as a dashed horizontal line. RAAN = Right Ascension Of Ascending Node.

spacecraft orbit. In other words, uncertainties in the predictions of the thermospheric density have an effect on the probability of collision.

4.2. Effects of Uncertainties in the Thermospheric Density Predictions on the Probability of Collision

SpOCK was run to assess the risk of collision between two hypothetical objects using the algorithm presented in section 2. Both spacecraft orbited at 400 km with a 30° and 60° inclination, respectively. The ECI states and covariance matrices at the initial epoch (12 a.m. universal coordinated time on 26 November 2016) are included in Appendix A. A first collision risk assessment was performed using the median values of the F10.7 and A_p predictions of Figure 3 (bin centered at 0 in green), so the density was modeled using the predictions of F10.7 and A_p by SWPC. The 50,000 ensemble members were propagated for each of the two satellites, so the total number of possible encounters was 2.5 billion. The orbits were propagated with a 10-s time step, and the gravitational perturbation due to the equatorial bulge (J_2) was taken into account. The green line in Figure 6 (top left) represents the orbit of Satellite 1 (30° inclination) and the magenta line represents the orbit of Satellite 2 (60° inclination). The closest approach was predicted to occur over the Pacific Ocean.

The relative distance over the first 2 days between the two unperturbed orbits is presented in the bottom plot of Figure 6. The time of closest approach was predicted to occur $\sim 36 \text{ hr}$ after epoch, at noon on 27 November.

A zoom in of the encounter geometry is illustrated in Figure 6 (top right). Three 10-s time steps are represented around the time of closest approach. Object 1 is represented by green squares (smaller inclination) and Object

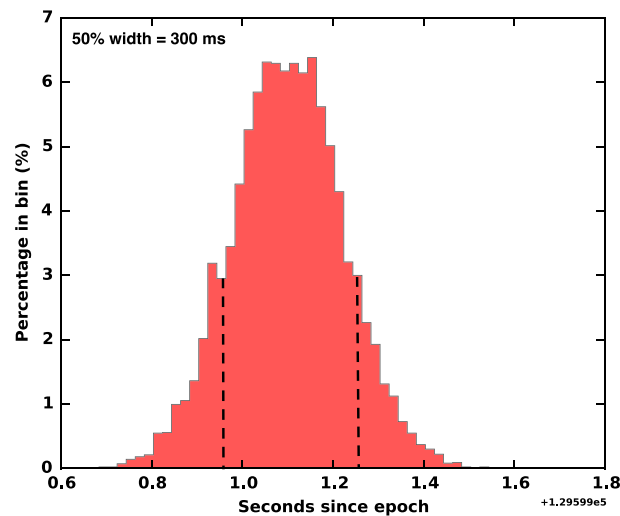


Figure 7. Distribution of the time of close approach for all conjunctions. The 25% and 75% quantiles are shown as vertical dashed lines.

2 by magenta circles (higher inclination). The time of closest approach was predicted to be at 12:00:00.104, at $\sim 21.75^\circ\text{N}$ latitude.

The minimum distance under which a close approach between the two unperturbed orbits was flagged was 10 km. Because this occurred, SpOCK's Monte Carlo algorithm presented in section 2.1 assessed the risk of collision for this possible conjunction. The sum of the two spacecraft radii was 1.3 m, implying that any situation with a distance between an object $O_{m,1}$ and an object $O_{n,2}$ smaller than 1.3 m was recorded as a collision.

When this was completed, the probability of collision was 1.051×10^{-4} , right above the threshold for a collision avoidance maneuver (10^{-4}) used by NASA (this threshold varies by individual NASA mission, though). The distribution of the time of closest approach for each collision between a perturbed object $O_{m,1}$ and a perturbed object $O_{n,2}$ is shown in Figure 7. The 50% width of the distribution (defined as the difference between the 75% and the 25% quantiles) is ~ 300 ms, which represents the uncertainty in the time of closest approach. This uncertainty is particularly small because of the encounter geometry. For example, if the inclinations of the two orbits were similar, the velocities at conjunction would be almost parallel to each other. Since uncertainties are usually greater in the along-track direction, the range of values for the time of close approaches increases for such parallel conjunctions.

To demonstrate the effects of uncertainties in the thermospheric density on the probability of collision, the risk of collision was assessed with the different densities shown in Figure 4. More specifically, 49 cases were evaluated for collision risk assessment. Each case corresponded to the probability of collision between the two objects orbiting in an atmosphere whose density was represented by one of the 49 scenarios of Figure 4.

The time and distance of closest approach between the two unperturbed orbits, that is, using the nominal orbital parameters, for nine cases are represented in Table 1. These cases correspond to example trajectories that were generated by moving the F10.7 and Ap prediction errors in lock step through the whole range of errors in order to span the entire spectrum of possibilities. The unperturbed orbits were not predicted to collide because the distances at closest approach were greater than 1.3 m, but they were flagged to be investigated due to the distances being less than 10 km.

The higher the density, the more drag there is on the spacecraft, which leads to a lower orbital altitude and thus a higher orbital speed, resulting in earlier closest approaches. This can be noticed in Table 1 where the time of close approach gradually decreased from Case 1 (lowest densities) to Case 9 (highest densities) by ~ 400 ms.

Figure 8 shows the positions of the two spacecraft on 27 November at 12:00:00 for the nominal orbit condition for these nine different thermospheric conditions. This corresponds to the time step preceding the close approach for all cases, except for Cases 8 and 9, for which it corresponds to the time step following the encounter. The increasing delay between this snapshot and the encounter from Case 1 to Case 7 is evident

Table 1*Time and Distance of Close Approach for Different Atmospheric Density Scenarios*

Case #	TCA	DCA (m)
1	2016-11-27 12:00:00.311	125
2	2016-11-27 12:00:00.213	106
3	2016-11-27 12:00:00.182	91.2
4	2016-11-27 12:00:00.124	64.3
5	2016-11-27 12:00:00.104	58.0
6	2016-11-27 12:00:00.075	42.6
7	2016-11-27 12:00:00.047	26.7
8	2016-11-27 11:59:59.989	1.61
9	2016-11-27 11:59:59.914	38.2

Note. TCA = Time of Close Approach; DCA = Distance of Close Approach.

in Figure 8. Because the closest approach for Cases 8 and 9 occurred before the time of this snapshot, the red and purple markers are located beyond the conjunction point (not represented in the Figure for clarity).

Added to the uncertainty of the time of closest approach between ensembles of the same scenario (e.g., 300 ms, Figure 7), the total uncertainty on the time of close approach, including uncertainties in the thermospheric densities, was ~ 700 ms. This is a small uncertainty and it does not cause any concern for operations because maneuvers are planned hours in advance. However, this short uncertainty was due to the encounter geometry, where the two objects approach with nonparallel velocities. For parallel conjunctions, this uncertainty would grow dramatically.

Although the effects of density uncertainties on the time of closest approach were small for this geometrical configuration, the effects on the probability of collision were much more important. The likelihood of each of the 49 density scenarios to occur at TCA is given as the product of the likelihood of the prediction error in F10.7 to occur at TCA with the likelihood of the prediction error in Ap to occur at TCA, since the distributions of the historical prediction errors of F10.7 and Ap are uncorrelated. Since the temporal resolution of the F10.7 and Ap predictions was 1 day, the likelihoods of the prediction errors in F10.7 and Ap were evaluated at +48h, instead of +36h (TCA). For instance, the likelihood of the error in F10.7 and Ap to be 9 and -4 , respectively (red and light blue bins of the PDFs in Figure 3, respectively) was $0.07 \times 0.16 \approx 0.011$. In other words, the likelihood of occurrence of the density scenario modeled by NRLMSISE from the F10.7 and Ap values depicted in red and light blue in the right two graphs of Figure 3 was $\sim 1.1\%$. Each of the 49 density scenarios in Figure 4 occurred with a probability computed with the same method, resulting in 49 values of the probability of collision, which likelihood to occur was equal to the likelihood of occurrence of the corresponding density scenario. Figure 9 (left) shows the PDF of the probability of collision derived from the 49 values of P_c and their likelihood

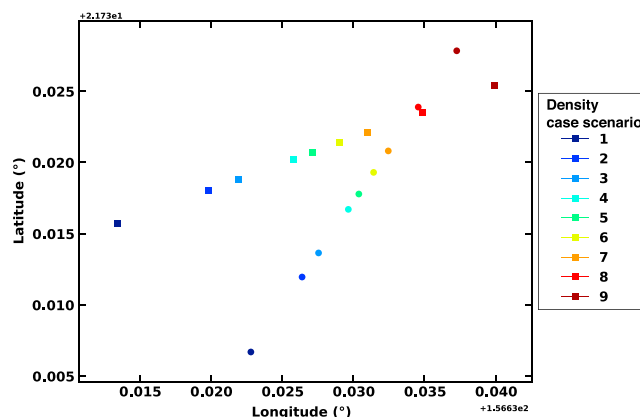


Figure 8. Snapshot of the unperturbed orbits \bar{O}_1 (square) and \bar{O}_2 (circle) at 12:00:00 p.m. on 27 November 2016. The two objects are about to collide for Cases 1–7 and have just collided for Cases 8 and 9.

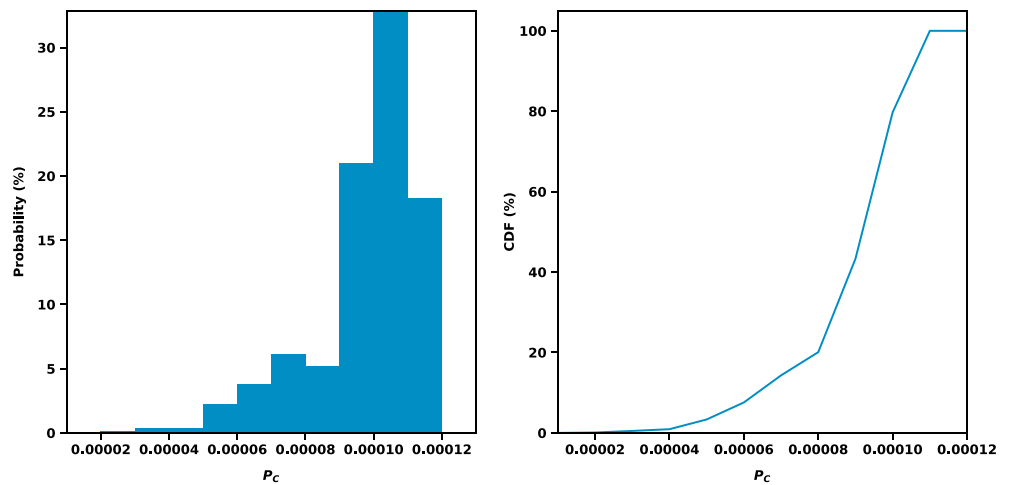


Figure 9. Probability distribution function and cumulative distribution function of P_c as a result of uncertainties in the atmospheric density. The probability distribution function and cumulative distribution function were segmented into bins of P_c of 10^{-5} .

of occurrence. The probability of each P_c interval to occur is equal to $\sum_i P_{c,i} \times p_i$ (for all $P_{c,i}$ in the interval), where p_i is the likelihood of the probability $P_{c,i}$ to occur. The peak of the PDF was obtained for P_c between 1.0×10^{-4} and 1.1×10^{-4} , for which the probability of occurrence was larger than 30%. The cases with a probability of collision falling in this interval corresponded to densities modeled from values of F10.7 and A_p close to the SWPC predictions since these were the most likely to occur, as shown in the distributions of Figure 3. The PDF extended to values of P_c as low as $\sim 10^{-5}$, although probabilities of occurrence of such scenarios were much lower ($<5\%$). Overall, the expected probability of collision, equal to the sum of each P_c to occur multiplied by its likelihood of occurrence, was 8.7×10^{-5} , right below the maneuver threshold used by NASA. Figure 9 (right) shows the CDF of the probability of collision. The CDF gives the probability of P_c to be below a certain threshold. For instance, the probability for P_c to be below 8×10^{-5} or 10^{-4} was $\sim 25\%$ or $\sim 85\%$, respectively. While PDFs indicate the values of P_c that are the most likely to occur, CDFs can help identify how much of the probability density is above or below a certain threshold.

This analysis shows that uncertainties in the prediction of the thermospheric density can lead to important errors on the probability of collision if only the nominal prediction is considered for the collision risk assessment, even if the conjunction occurs only 36 hr after the current epoch. More importantly, it provides

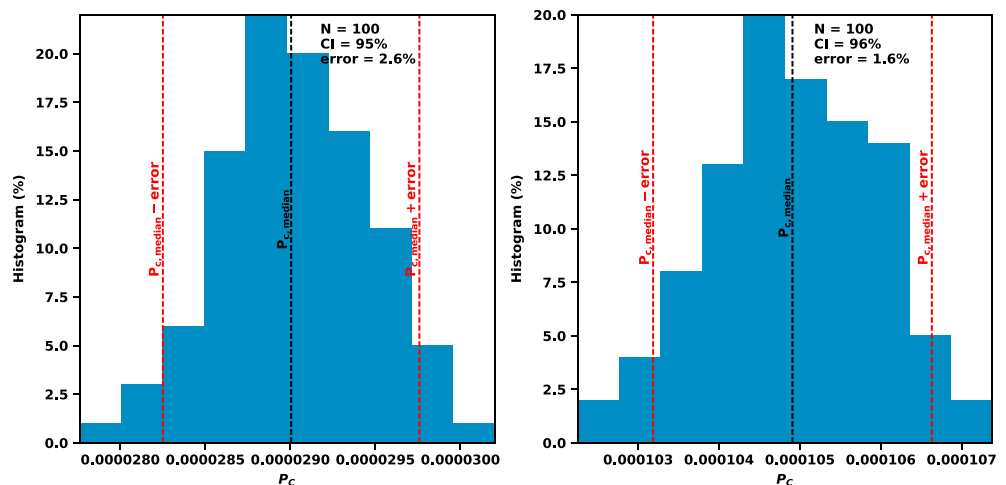


Figure 10. Distribution of the 100 estimated values of P_c (left: $\sim 3 \times 10^{-5}$; right: $\sim 1 \times 10^{-4}$). The confidence interval and relative error are indicated. The red dashed lines correspond to the boundaries of the interval that included $\sim 95\%$ of the predicted values of P_c . The black dashed lines represent the median values of the distributions.

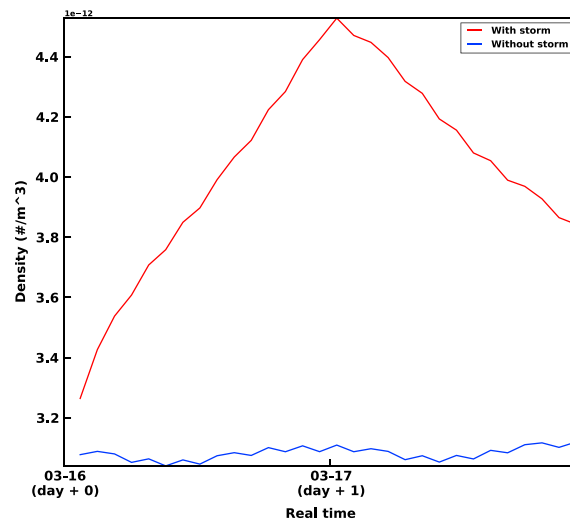


Figure 11. Orbit average density at the position of the spacecraft with the geomagnetic storm (red) and without the geomagnetic storm (blue).

an example of application of a framework that can assist collision avoidance practitioners to estimate the risk of collision by providing a true probabilistic result for different P_c outcomes.

4.2.1. Confidence Interval

An empirical method was used to compute the confidence interval associated with the estimations of the probability of collision. The scenarios that gave the minimum and maximum values of P_c ($\sim 3 \times 10^{-5}$ and $\sim 1 \times 10^{-4}$, respectively) were considered to bound the solution. For each of these two scenarios, SpOCK was run 100 times and the confidence interval was computed from the distribution of the 100 P_c values. Figure 10 shows the distributions corresponding to the 100 runs for the minimum value of P_c ($\sim 3 \times 10^{-5}$, left) and for the maximum value of P_c ($\sim 1 \times 10^{-4}$, right). For each distribution, the median value of P_c was computed, $P_{c,median}$, and the relative error on P_c , ϵ , was derived to include $\sim 95\%$ of the P_c values in the interval $[P_{c,median} \times (1 - \epsilon), P_{c,median} \times (1 + \epsilon)]$. Approximately 95% of the runs resulted in probabilities of collision different by less than 2.6% compared to the median value of the lowest probability of collision ($\sim 3 \times 10^{-5}$) and by less than 1.6% compared to the median value of the highest probability of collision ($\sim 1 \times 10^{-4}$). The larger distribution for the low value of P_c is consistent with the fact that more ensemble members should be run in order to get the same relative error as for the scenario with the larger value of P_c . The 47 other scenarios resulted in probabilities of collision between these two P_c extrema, so the relative error corresponding to a confidence interval of 95% for these scenarios was between 1.6% and 2.6%. Overall, although this empirical method is an approximation, it provides an estimation of the confidence interval and shows that the Monte Carlo approach used to compute the probability of collision for the previous example scenarios was relevant.

4.3. Probability of Collision Errors Due To a Miss Prediction of a Solar Storm

In the previous section, the probability of collision was assessed given uncertainties in the thermospheric density during quiet conditions. In this section, the impact of a geomagnetic storm on the probability of collision is investigated. For this analysis, the geomagnetic storm occurring on 17 March 2015 was studied. Two orbits were propagated for 2 days, starting on 16 March. The encounter geometry corresponded to a parallel path conjunction: both orbits were at an inclination of 45° at 400 km. The eccentricity of Object 2 is slightly higher than the eccentricity of Object 1 (0.00002 and 0.00001, respectively). This is a particularly interesting configuration as the assumption of short time of encounter used in many collision risk assessment algorithms does not hold for this parallel conjunction geometry.

The geomagnetic index A_p was reported to reach values as high as 200 on 17 March. The orbit-averaged density modeled at the position of Object 1 using NRLMSISE is shown in Figure 11. The red line shows the density modeled from the actual F10.7 and A_p , while the blue line represents the density modeled with keeping F10.7 and A_p constant to the initial value on 16 March.

To study the effect of the storm on the probability of collision, two conjunction analysis simulations were made. The first one used the actual solar activity conditions to model the atmospheric density (red line

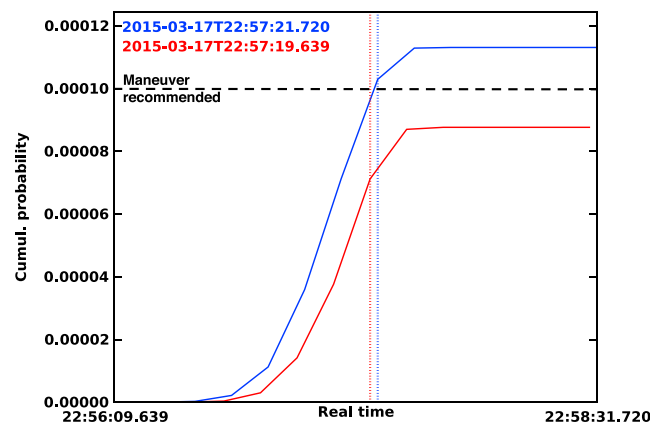


Figure 12. Cumulative probability of collision as a function of time during the encounter. The scenario with the storm is in red and without the storm in blue. The vertical dashed lines represent the times of closest approach between the unperturbed orbits (indicated on the top left corner). The collision avoidance maneuver threshold (10^{-4}) is represented with a black dashed line.

in Figure 11). The second one used a constant solar activity for the 2 days of the simulations (blue line in Figure 11). This simulation corresponded to a situation without a geomagnetic storm, as if the predictions were for calm geomagnetic conditions instead of for a storm. For both runs, the risk of collision was assessed by SpOCK to compare the probability of collision and the time of conjunction.

Figure 12 shows the cumulative PDF as a function of time for both simulations, defined as the total number of recorded collisions as a function of time, divided by the total number of possible conjunctions. Consequently, the total cumulative probability of collision at the end of the span is equal to the probability of collision N_T/N used so far in the study. The red line corresponds to the simulation with the geomagnetic storm, and the blue line without it. The vertical dashed lines represent the times of closest approach between the unperturbed orbits, which are also indicated in the top left corner of the plot.

The conjunction occurred sooner in the presence of the storm by ~ 2 s. This was due to a stronger drag because of the increase in density resulting from the effects of the geomagnetic storm on the thermosphere. Therefore, the satellites orbited with higher velocities and the close approach occurred sooner than without the storm.

The probability of collision in the absence of the storm was slightly above the maneuver threshold (1.13×10^{-4}); however, with the storm, the probability of collision was 8.80×10^{-5} , which was under the maneuver threshold. This $\sim 30\%$ difference in the probability of collision not only demonstrates the important effect of the storm on the probability of collision but it also shows that if on 16 March, the space weather models had not predicted the storm to occur a day later, the predicted probability of collision would have been right above the maneuver threshold so the mission operator may have been advised to perform a collision avoidance maneuver. This miss prediction of the storm would have led to a false alert, which means that the maneuver may have unnecessarily been carried out and might have led to a riskier, rather than safer, outcome. This approach is not specific to this storm but can be applied to storms in general, showing that a storm can possibly change the probability of collision, which can also result in making the wrong decision with regard to a collision avoidance maneuver, in one direction or the other.

The minimum distance between the objects used to flag a collision also has an influence on the effects of the storm on the probability of collision. This is investigated in Table 2. The effects of the geomagnetic storm increased with decreasing minimum distance of collision: the relative difference in the probability of collision increased with decreasing minimum distance (so did the absolute difference, not shown in Table 2).

The storm perturbed the orbits by increasing the distance at closest approach between two objects in some cases and by decreasing the distance at closest approach between two objects in other cases, as explained in section 4.1. The decrease in probability of collision shows that taking into account all possible conjunctions, the storm overall decreased the total number of encounters in this particular example. In other words, there were more cases where it increased the distance at closest approach from a value below the minimum distance (without the storm) to a value above the minimum distance (with the storm) than cases where it

Table 2
Probability of Collision With and Without the Geomagnetic Storm for Different Values of the Minimum Distance of Collision

Min distance collision (m)	P_c with storm	P_c without storm	Relative difference
5	0.001701	0.001559	9.1%
2	0.000338	0.000276	22.5%
1.2	0.000113	0.000088	28.4%
1.0	0.000073	0.000056	30.4%

decreased the distance at closest approach from a value above the minimum distance (without the storm) to a value below the minimum distance (with the storm).

The fact that the probability decreased more as a result of lowering the minimum distance of collision in the presence of a storm (Table 2) means that the number of conjunctions decreased more with the storm than without the storm if the minimum distance of collision was smaller. To understand why, consider a situation where the storm increased the distance at closest approach from 1.5 m (without the storm) to 4 m (with the storm). The situation is recorded as a collision with and without the storm if the minimum distance of collision was 5 m. If the minimum distance instead was 2 m, this situation would still be recorded as a collision without the storm but it would not be recorded anymore as a collision with the storm. In other words, the total number of collisions without the storm would still be the same with the new threshold but it would be smaller by one conjunction in the presence of the storm.

Consequently, for lower probability of collisions (10^{-5} , 10^{-6} , for instance), the relative difference is expected to be even greater. An application of this study is that there is often an unknown on the minimum distance of collision to set for the evaluation of the probability of collision. Recall that this distance corresponds to the sum of the two object radii only if the objects are spherical, which is not the case most of the time, particularly if the objects are satellites. Satellites can also have tethers or booms, such as the Challenging Mini-satellite Payload satellite. Therefore, the attitude of the satellite has a direct influence on the minimum distance of collision. Unfortunately, a perfect knowledge of the attitude is almost always impossible, since the vast majority of objects in orbit have uncertain geometries and orientations, resulting in uncertainties on the minimum distance of collision. This analysis shows that the effects of a miss prediction of a storm can possibly vary with the attitude of the spacecraft at the time of closest approach.

5. Conclusion

The CARA algorithm developed in SpOCK uses a Monte Carlo approach to predict the probability of collision from the covariance matrices of the two objects at epoch. SpOCK propagates ensemble members, representing small perturbations on the initial positions and velocities, by modeling the perturbing forces such as the perturbations of the gravitational potential due to the asphericity and nonuniform mass distribution of the Earth, the atmospheric drag, the solar radiation pressure, and the gravitational perturbations from the Moon and the Sun. More specifically, it uses a thermosphere model, either NRLMSISE or Global Ionosphere Thermosphere Model, to accurately model the atmospheric density at the position of the spacecraft, hence the drag acceleration. While propagating the perturbed orbits, SpOCK screens for collisions between all ensemble members. Specifically, it interpolates the minimum distance between two objects with fifth-order polynomials. If this distance is smaller than the sum of the two object radii, it records the situation as a conjunction. After repeating this operation for all ensemble members, SpOCK divides the total number of encounters by the total number of cases, usually at least a hundred million, which approximates the probability of collision.

Although atmospheric drag is one of the main perturbing forces for LEO orbits (representing 90% to 95% of the force in the in-track direction), uncertainties in the thermospheric density are usually not taken into account in collision risk assessment algorithms. Important uncertainties rely on the atmospheric density because the coupling of the upper atmosphere with the Earth space environment (the ionosphere and the magnetosphere) is not well understood, and because the solar activity, the main driver of this coupled system, is itself very hard to predict. Coronal mass ejection, solar flares, and CIRs cause important and difficult to predict disturbances of the atmospheric density. Therefore, ignoring all these effects results in important errors in the prediction of the probability of collision. The approach for taking into account the uncertainties in the solar activity to derive PDFs of the probability of collision was introduced. Specifically, PDFs and CDFs of

the probability of collision can be derived from distributions of historical forecast errors in the geomagnetic indices F10.7 and Ap. An example of such a PDF was provided for a simulated conjunction and illustrated variations in the probability of collision of an order of magnitude. These PDFs and CDFs can assist operators in the determination of the true risk of collision in the presence of atmospheric density errors. An empirical method to determine the confidence interval associated with the predictions of the probability of collision was presented and showed that 95% of the runs resulted in values of the probability collision less than 2.6% different from the median value. Although the Monte Carlo method was used in this study to predict the probability of collision, the overall approach is applicable to other methods, such as analytical methods.

Finally, the effects of geomagnetic storms on the probability of collision were illustrated with an example of a parallel conjunction between two spacecraft 2 days after epoch. On 17 March 2015, a strong storm hit the upper atmosphere, with values of the geomagnetic index Ap exceeding 200. Density enhancements by almost 50% at 400 km strongly increased the drag, modifying the orbits of the satellites. The effects on the risk of collision led to differences up to 30% in the probability of collision, compared to a situation without a storm. This relative difference was shown to vary inversely with the minimum distance (i.e., the size of the objects). This analysis demonstrates the importance of predicting geomagnetic storms. In this example, the miss prediction of the geomagnetic storm resulted in a false alert because the probability of collision without the storm was above the threshold for a collision avoidance maneuver.

Appendix A: Initial States and Covariance Matrices

Distances are expressed in meters, and time in seconds.

$$\bar{U}_{1,t_0} = \begin{pmatrix} 202780.692 \\ -5873336.722 \\ -3356137.888 \\ 7644.314213 \\ 540.915272 \\ -493.855868 \end{pmatrix} \quad (A1)$$

$$C_1 = \begin{pmatrix} 4.7440894789163000000000 & -1.2583279067770000000000 & -1.2583279067770000000000 & 0.00000000000000000000 & 0.00000000000000000000 & 0.00000000000000000000 \\ -1.2583279067770000000000 & 6.1279552605419000000000 & 2.1279552605419000000000 & 0.00000000000000000000 & 0.00000000000000000000 & 0.00000000000000000000 \\ -1.2583279067770000000000 & 2.1279552605419000000000 & 6.1279552605419000000000 & 0.00000000000000000000 & 0.00000000000000000000 & 0.00000000000000000000 \\ 0.0000000000000000000000 & 0.00000000000000000000 & 0.00000000000000000000 & 0.00000100000000000000 & 0.00000000000000000000 & 0.00000000000000000000 \\ 0.0000000000000000000000 & 0.00000000000000000000 & 0.00000000000000000000 & 0.00000000000000000001 & 0.00000100000000000000 & -0.00000000000000000001 \\ 0.0000000000000000000000 & 0.00000000000000000000 & 0.00000000000000000000 & 0.00000000000000000001 & -0.00000000000000000001 & 0.00000100000000000000 \end{pmatrix} \quad (A2)$$

$$\bar{U}_{2,t_0} = \begin{pmatrix} 558232.011 \\ -3649646.379 \\ -5675244.936 \\ 6569.617992 \\ 3593.547352 \\ -1664.494700 \end{pmatrix} \quad (A3)$$

$$C_2 = \begin{pmatrix} 4.7439512624715000000000 & -1.2582550000046000000000 & -1.2582079265320000000000 & 0.00000000000000000000 & 0.00000000000000000000 & 0.00000000000000000000 \\ -1.2582550000046000000000 & 6.1281039832865000000000 & 2.1280243672750000000000 & 0.00000000000000000000 & 0.00000000000000000000 & 0.00000000000000000000 \\ -1.2582079265320000000000 & 2.1280243672750000000000 & 6.1279447542420000000000 & 0.00000000000000000000 & 0.00000000000000000000 & 0.00000000000000000000 \\ 0.0000000000000000000000 & 0.00000000000000000000 & 0.00000000000000000000 & 0.00000100000000000000 & 0.00000000000000000000 & 0.00000000000000000000 \\ 0.0000000000000000000000 & 0.00000000000000000000 & 0.00000000000000000000 & 0.00000000000000000000 & 0.00000100000000000000 & -0.00000000000000000002 \\ 0.0000000000000000000000 & 0.00000000000000000000 & 0.00000000000000000000 & 0.00000000000000000000 & -0.00000000000000000002 & 0.00000100000000000000 \end{pmatrix} \quad (A4)$$

Acknowledgments

This research was funded by NASA grant NNL13AQ00C and was supported by AFOSR under DDDAS (Dynamic Data-Driven Applications Systems, <http://www.1dddas.org/>) grant FA9550-16-1-0071. We acknowledge use of NASA/GSFC's Space Physics Data Facility's OMNIWeb service and OMNI data, the Space Weather Prediction Center data from the National Oceanic and Atmospheric Administration, and the use of the Satellite Tool Kit (STK) at Analytical Graphics, Inc. for the visualization of orbits. The data used are listed in the references, tables, and appendix.

References

- Aida, S., Kirschner, M., & Meissner, F. (2015). Collision risk assessment and mitigation strategy for the GSOC GEO satellites. In *24th International Symposium on Space Flight Dynamics*. Laurel, MD.
- Akella, M. R., & Alfriend, K. T. (2000). Probability of collision between space objects. *Journal of Guidance, Control, and Dynamics*, 23(5), 769–772.
- Alfano, S. (1994). Determining satellite close approaches. *Journal of the Astronautical Sciences*, 42, 143–152.
- Alfano, S. (2005a). A numerical implementation of spherical object collision probability. *Journal of the Astronautical Sciences*, 53(1), 103–109.
- Alfano, S. (2005b). Beta conjunction analysis tool. In *AAS/AIAA Astrodynamics Specialist Conference* (pp. 2245–2256). Mackinac Island, MI.
- Alfano, S. (2006). Addressing nonlinear relative motion for spacecraft collision probability. In *AAS/AIAA Astrodynamics Specialist Conference* (pp. 6760). Keystone, CO.
- Alfano, S. (2009). Satellite conjunction Monte Carlo analysis. In *AAS Spaceflight Mechanics Mtg* (pp. 09–223). Savannah, GA.
- Alfriend, K. T., Akella, M. R., Frisbee, J., Foster, J. L., Lee, D.-J., & Wilkins, M. (1999). Probability of collision error analysis. *Space Debris*, 1(1), 21–35.
- Bruinsma, S. L., & Forbes, J. M. (2007). Global observation of traveling atmospheric disturbances (TADS) in the thermosphere. *Geophysical Research Letters*, 34, L14103. <https://doi.org/10.1029/2007GL030243>
- Bruinsma, S., Forbes, J. M., Nerem, R. S., & Zhang, X. (2006). Thermosphere density response to the 20–21 November 2003 solar and geomagnetic storm from CHAMP and GRACE accelerometer data. *Journal of Geophysical Research*, 111, A06303. <https://doi.org/10.1029/2005JA011284>
- Bussy-Virat, C., Getchius, J., & Ridley, A. (2018). The spacecraft orbital characterization kit and its applications to the CYGNSS mission. In *2018 Space Flight Mechanics Meeting* (pp. 1973). <https://doi.org/10.2514/6.2018-1973>
- Chan, F. (2008). *Spacecraft collision probability*. Reston, VA: Aerospace Press.
- Emmert, J. (2015). Thermospheric mass density: A review. *Advances in Space Research*, 56(5), 773–824.
- Emmert, J., Byers, J., Warren, H., & Segerman, A. (2014). Propagation of forecast errors from the Sun to LEO trajectories: How does drag uncertainty affect conjunction frequency? (Tech. Rep.) DTIC Document.
- Emmert, J., Warren, H., Segerman, A., Byers, J., & Picone, J. (2016). Propagation of atmospheric density errors to satellite orbits. *Advances in Space Research*, 59(1), 147–165.
- Foster, J. (2001). The analytical basis for debris avoidance operations for the International Space Station. *Orbital Debris Quarterly News*, 6(2), 11.
- Hejduk, M., & Frigm, R. (2015). Collision avoidance short course—Part I: Theory. In *NASA robotic CARA*. Greenbelt, MD.
- Horsley, M. (2012). Satellite re-entry modeling and uncertainty quantification. In *Advanced Maui Optical and Space Surveillance Technologies Conference*. Vol. 1, (p. 52).
- Lei, J., Thayer, J. P., Wang, W., & McPherron, R. L. (2011). Impact of cir storms on thermosphere density variability during the solar minimum of 2008. *Solar Physics*, 274(1-2), 427–437.
- Liou, J.-C. (2016). The orbital debris problem. In *Space Tech Conference*. Pasadena, CA.
- Moe, K., & Moe, M. M. (2005). Gas surface interactions and satellite drag coefficients. *Planetary Space Science*, 53, 793–801. <https://doi.org/10.1016/j.pss.2005.03.005>
- Newman, L. K. (2016). NASA conjunction assessment risk analysis approach. *NASA robotic CARA*.
- Pachura, D., & Hejduk, M. D. (2016). Conjunction assessment late-notice high-interest event investigation: Space weather aspects. In *NASA robotic CARA*. Greenbelt, MD.
- Patera, R. P. (2001). General method for calculating satellite collision probability. *Journal of Guidance, Control, and Dynamics*, 24(4), 716–722.
- Patera, R. P. (2005). Calculating collision probability for arbitrary space vehicle shapes via numerical quadrature. *Journal of Guidance, Control, and Dynamics*, 28(6), 1326–1328.
- Pawłowski, D. J., & Ridley, A. J. (2011). The effects of different solar flare characteristics on the global thermosphere. *Journal of Atmospheric and Solar-Terrestrial Physics*, 73(13), 1840–1848.
- Picone, J., Hedin, A., Drob, D. P., & Aikin, A. (2002). NRLMSISE-00 empirical model of the atmosphere: Statistical comparisons and scientific issues. *Journal of Geophysical Research*, 107(A12), 1468. <https://doi.org/10.1029/2002JA009430>
- Ridley, A., Deng, Y., & Toth, G. (2006). The global ionosphere-thermosphere model. *Journal of Atmospheric and Solar-Terrestrial Physics*, 68(8), 839–864.
- Sanchez-Ortiz, N., Domínguez-González, R., Krag, H., & Flohrer, T. (2015). Impact on mission design due to collision avoidance operations based on TLE or CSM information. *Acta Astronautica*, 116, 368–381. <https://doi.org/10.1016/j.actaastro.2015.04.017>
- Schilling, B., Taleb, Y., Carpenter, J. R., Balducci, M., & Williams, T. W. (2016). Operational experience with the Wald Sequential Probability Ratio test for conjunction assessment from the Magnetospheric Multiscale Mission. In *AIAA/AAS Astrodynamics Specialist Conference* (pp. 5424).
- Stoll, E., D'Souza, B., Virgili, B. B., Merz, K., & Krag, H. (2013). Operational collision avoidance of small satellite missions. In *Aerospace Conference, 2013 IEEE* (pp. 1–11). <https://doi.org/10.1109/AERO.2013.6496955>
- Storz, M. F., Bowman, B. R., Branson, M. J. I., Casali, S. J., & Tobiska, W. K. (2005). High accuracy satellite drag model (HASDSM). *Advances in Space Research*, 36(12), 2497–2505.
- Sutton, E. K., Forbes, J. M., & Nerem, R. S. (2005). Global thermospheric neutral density and wind response to the severe 2003 geomagnetic storms from CHAMP accelerometer data. *Journal of Geophysical Research*, 110, A09S40. <https://doi.org/10.1029/2004JA010985>
- Sutton, E. K., Forbes, J. M., Nerem, R. S., & Woods, T. N. (2006). Neutral density response to the solar flares of October and November, 2003. *Geophysical Research Letters*, 33, L22101. <https://doi.org/10.1029/2006GL027737>
- Vallado, D. A., & Finkleman, D. (2014). A critical assessment of satellite drag and atmospheric density modeling. *Acta Astronautica*, 95, 141–165. <https://doi.org/10.1016/j.actaastro.2013.10.005>
- Vallado, D., & McClain, W. (2007). *Fundamentals of astrodynamics and applications* (3rd ed.). New York: Space Technology Library, Microcosm Press and Springer.